Journal of the Korean Nuclar Society
Volume 4, Number 2, June, 1972

≪Original≫ A Fast Neutron Time-of-Flight Spectrometer with High Resolution

Cho, Mann

Physics Division, Atomic Energy Research Institute, Seoul, Korea

(Received May 1. 1972)

Abstract

A fast neutron time-of-flight spectrometer has been constructed with suitable choice of target thickness and proton bombarding energy in $Li^7(p, n)$ Be^7 nuclear reaction for a continuous keV spectrum of neutrons at 0 degree in 1-nsec pulse from a Van de Graaff and a time-pick-up fast neutron detector assembled with a 5 mm-thick 92% enriched B^{10} slab and four heavily shielded 4″×3″ NaI scintillation detectors.

Energy resolution of this spectrometer is better than 0.3% at 50 keV and the signal-to-background ratio is also improved. Total cross section measurements of several separated single isotopes have been carried out with this spectrometer and analyzed by Rmaxtrix multi-level computer code. The spin values and resonance parameters of each individual resonances are given.

요 약

$Li^7(p, n)$ Be^7 原子核反應에서 Li target의 두께와 入射陽子의 에너지를 적절히 選定하므로써 1-n sec 脈動 Van de Graaff 加速器로 부터 keV 領域에서의 連續中性子 spectrum 을 發生 시키고 92% 濃縮된 5mm 두께의 B^{10} 板과 4개의 4″×3″ NaI (Tl) 螢光體로 이루어진 速中性子檢出器를 利用 速中性子 飛行時間法에 依한 中性子 spectrometer 를 製作하였다.

裝置의 에너지 分解能은 50 keV 에서 0.3%보다 良好하며 信號對雜音比도 改良 되었다. 이를 利用하여 몇가지 分離된 單一同位元素의 全斷面積을 測定하고 R-matrix 電子計算 code 로 解析하였다. 각 共鳴에 따르는 스핀値와 共鳴因數들을 찾아 내었다.

1. Introduction

High resolution neutron time-of-flight spectrometers in the keV-region are of interest, both for the construction of fast breeders, and for the investigation of physical questions.

Nevertheless, the existing data are still quite unsatisfactory due to the difficulties of high resolution spectroscopy in this energy range. Good *et al*[1]. have measured the parameters of 18 resonances of Ti^{47} and 17 resonances of Ni^{61} up to 50 keV. Measurements at higher energies were performed with the Cyclotron of the Columbia University by Grag et al.[2]. Spin value have not been assigned and the area analysis which can not discribe

the interference effects between the close resonances were used by these workers.

For studying the interaction of neutrons with nuclei, neutrons of well-defined energies are required. This paper describes a fast neutron time-of-flight spectrometer with techniques specifically designed to cover the energy range 8 to 80 keV. The method employs a 1-nsec bursts of neutrons from the Li^7 (p, n) Be^7 reaction produced by a pulsed beam from a 3-MeV Van de Graaff[3]. By sutable choice of target thickness and proton bombarding energy, a spectrum of neutrons is produced at O° to the proton beam for covering part or all of the kilovolt region to be studied.

These unmoderated neutrons constitute the source from which energies are chosen by time-of-flight measurements. The technique is therefore a combination of the Van de Graaff and time-of-flight techniques in which the Van de Graaff supplies only the required spectrum of neutrons and the time-of-flight measurement establishes the precise energy.

For the lower energy region up to 80 keV the B^{10} slab detectors are used. Around the boron slab four well-shielded NaI(Tl) detectors were mounted perpendicular to the neutron beam. With this arrangement the background is not time-correlated and can be measured in a very simple and accurate manner, The instrumental time resolution for the four parallel-conneted NaI(Tl) detectors was measured as 0.5 nsec/m with the 478 kev γ-ray from the lithium target.

For the analysis of measured cross sections R-matrix multi-level formulas are required which can describe the level-level interference effects due to overlapping resonances of the same spin state. To get reliable resonance parameters for not completely resolved resonance, these multi-level formulas should also include resolution effects. A precise knowledge of the spectrometer-resolution is thus important.

2. Experimental Arrangement

1) Time-of-Flight Technique

Very largely on account of the development of fast, highly efficient neutron detectors, short burst (in order of nsec) pulsed accelerators, and the adoption of computer techniques to the storage and display of information, the measurement of neutron energy by direct determination of velocity is being successfully extended into the keV range of energies.

The problem of time-of-flight measurement and analysis is essentially that of the measurement of ellapsed time between a reference time and the time of the events and much of the technique developed for coincidence study may be applied directly.

Let a neutron source emit short neutron pulses with a broad energy distribution. Let the neutron detector be at a distance l from the source. Since neutrons of energy E require a time

$$t=l/V=l/\sqrt{2E/M} \qquad (1)$$

to traverse the flight path, a unique relation exists between energy and the arrival time of the neutrons at the detector, providing only that the length of the neutron pulse is small compared to the time of flight. In this way, energy measurements on neutrons from a continuous source are possible. Since in place of the detector one can use another measuring instrument and detect the nuclear reactions caused by the neutrons, one can investigate neutron reactions in the same way as with purely monoenergetic sources.

In practice, the detector is connected to a "multi-channel analyzer" or "on-line computer", which separately registers the number of events ocuring in equal time intervals $t_{i+1}-t_i$; thus the entire spectrum can be obtained in one measurement. If the flight time is given in nsec, the flight path in meters, and the neutron energy in MeV, then the important relation

$$t(\text{nsec})=72.3\ 1(\text{meters})/\sqrt{E(\text{MeV})} \qquad (2)$$

holds. The accuracy with which energy measurements are possible with the time-of-flight method depends upon the uncertainty Δt in the flight time and Δl in the flight path(mainly detector thickness). As Δt is composed of the

pulse width of the neutron source as well as the time resolution of the detector and associated electronics, the relation

$$\frac{\delta E}{E}=2\sqrt{\frac{1}{2\sqrt{2ln2}}\cdot\frac{\Delta t}{t}\Big)^2+\Big(\frac{1}{\sqrt{12}}\cdot\frac{\Delta l}{l}\Big)^2} \quad (3)$$

holds.

The following facillities were used in this experiment.

1. Karlsruhe 10-nsec pulsed 3 MeV Van de Graaff accelerator with 1-nsec bunching system as the neutron source using the of $Li^7(p, n)Be^7$ nuclear reaction.
2. CAE-510 on-line computer for the data storage and handling.
3. LABEN time sorter and Analog-to-Digital Convertor as the time measuring equipment.
4. B^{10}-NaI fast neutron detector assembly with timing signal pick up electronics with fast-slow coincidence.
5. Automatic 4-position sample changer.
6. Miscellaneous equipment.

Fingure 1 shows the whole experimental facilities.

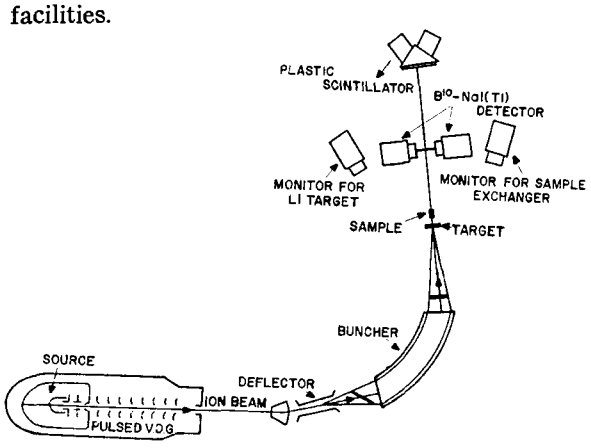

Fig. 1. Arrangement of experimental facilities

2) Li^7 (p, n) Be^7 Reaction as a Source of Unmoderated Neutrons

The important features of the $Li^7(p, n)Be^7$ reaction, so far as the present application is concerned, are (i) the yield with proton energy above neutron threshold, (ii) the dependence of the neutron energy on proton energy, and (iii) the energy dependence of the laboratory angular distribution. The neutron yield has been shown to rise rapidly at threshold because of a resonance[4]. In the neighborhood of threshold, the neutron energy and angular distribution vary rapidly with proton bombarding energy in a manner derivable from the mechanics of the center-of-mass motion. The equations are

$$E_n=\frac{M_nM_p}{(M_{Li}+M_p)^2}\times\Big\{E_p^{\frac{1}{2}}\cos\theta \pm\frac{M_{B_e}M_{Li}}{M_nM_p}(E_p-E_{th})-E_p\sin^2\theta\Big\} \quad (4)$$

$$\left|\frac{dN}{d\theta}\right|=\frac{2\pi\sin\theta}{Z}\alpha[\cos\theta\pm Z]^2 \quad (5)$$

$$\left|\frac{dE_n}{d\theta}\right|=2E_p\frac{\sin\theta}{Z}\frac{M_pM_n}{(M_p+M_{Li})^2}\times[\cos\theta\pm Z]^2 \quad (6)$$

$$\left|\frac{dN}{dE_n}\right|=\frac{dN/d\theta}{dE_N/d\theta}=\pi(M_p+M_{Li})^2\times[M_nM_pM_{Li}M_{B_e}E_p(E_p-E_{th})]^{-\frac{1}{2}} \quad (7)$$

where

M: Mass
E_p: proton energy
E_n: neutron energy
E_{th}: reaction threshold energy
N: number of neutrons
θ: angle between the proton beam and neutron beam direction

$$\alpha^2=\frac{M_nM_p}{M_{B_e}M_{Li}}\frac{E_p}{(E_p-E_{th})}$$

$$Z^2=\Big(\frac{1}{\alpha^2}-\sin^2\theta\Big)$$

The first equation shows the two-valued character of the neutron energy at each proton energy[5]. At the angle of 0° to the proton beam the lower branch of neutron energies ranges from 30 keV downwards, and is the group employed for the keV range of neutron energies. Equation 7 shows that near threshold the number of neutrons per energy interval increases as the bomarding energy approaches threshold from above. Equation 5 and Equa-

tion 6 show that this increase is the result of a forward concentration of the emitted neutrons as a consequence of center-of-mass motion. This concentration of neutrons into smaller angles as 30 keV is approached is partially compensated by the drop in yield as the bombarding proton energy is lowered toward threshold. It is an observed fact that, with targets a few keV thick and a detector substending about a 2° half-angle, the number of neutrons per energy interval actually increases approaching 30 keV. Thus, with the accompanying forward "focusing" it is possible to increase the flight path as the energy increases at no loss of counts per energy interval, and hence to cover the energy range 8 to 80 keV with constant fractional energy resolution. Because of the relatively short flight paths employed, it is very easy to keep the flight times of all neutrons approximately constant by varying the distance from target to detector. Figure 2 shows the primary neutron spectrum from targets of two different thicknesses. In this figure the high- and low-energy groups of neutrons are evident. Note the number of neutrons per unit energy interval for the two targets. This is predicated by Equation 7. A smooth, slowly varying neutron spectrum is highly desirable for cross section studies in order to minimize errors arising from slight spectrum shifts. Thus an ideal spectrum would be one that rises as rapidly

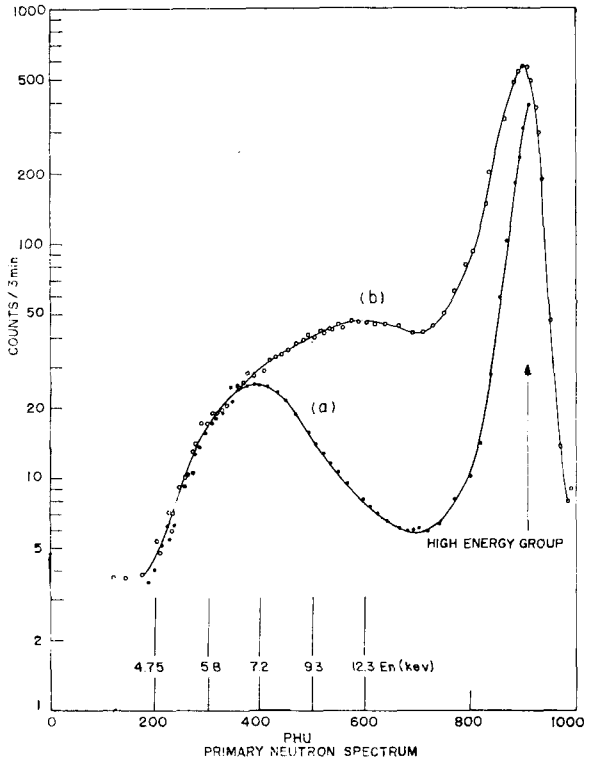

Fig. 2. Neutron yields from two thin lithium targets

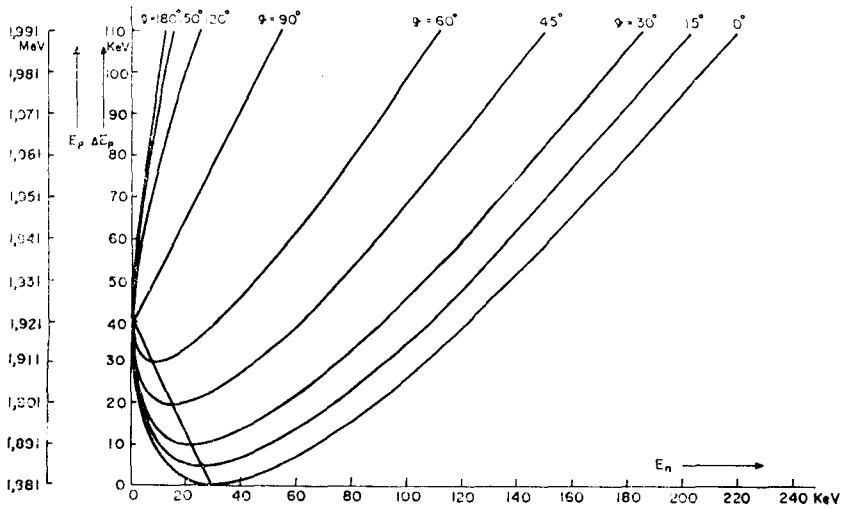

Fig. 3. Neutron energy distribution

as possible to plateau at the low-energy end, before rising on to the higher energy peak. Curve (b) of Figure 2 is a good approximation to this type of spectrum. Figure 3 shows neutron energy dependence on proton bombarding energy at several angle. It seems clear that it is desirable to reduce to a minimum the number of neutrons outside the energy region of interest. Hence, it is practical to employ targets whose thickness is just above that which corresponds to the maximum energy range desired.

The Li target of 20 keV thickness in maximum proton energy loss is evaporated on a nickel cap and soldered to a stainless steel Faraday cup, and attached to the beam tube by means of a Wilson seal.

3) Determination of Sample Position in Terms of In-scattering Correction

With any sample and detector of finite size, neutrons scattered forward in the sample toward the detector will be counted as if no interaction had occured. This in-scattering correction is minimized by using a small detector well-removed from the neutron source, and a sample just large enough to shadow the detector. This is referred to as a good geometry transmission measurement[6].

If one assumes a good-geometry set up the number of neutrons scattered in the sample between x and $x+dx$ which strike the detector is given by

$$[(Q/L_1^2)\exp(-n\sigma_T x)][(n\pi D^2/4)dx] \times[\sigma_n(0°)A/L_2^2][\exp(-n\sigma_T(t-x))] \quad (8)$$

where

t: the over-all length of the scattering sample, $t \ll L_1$ and L_2,

L_1: source-to-sample distance,

L_2: sample-to-detector distance,

Q: number of neutrons produced in the source in the direction of the sample per second per unit solid angle

D: diameter of cylindrical scattering sample of length t,

A: cross sectional area of the detector as seen from the source,

$\sigma_n(\varphi)$: differential elastic-scattering cross section for neutrons at the laboratory angle φ,

σ_t: true total cross section corrected for in-scattering,

σ_t': total cross section calculated neglecting in-scattering,

$L=L_1+L_2$: source-to-detector distance.

In this expression, the factors in brackets represent the flux at the depth x in the sample, the number of nuclei between x and $x+dx$, the differential cross section for elastic scattering in the forward direction times the solid angle of the detector subtended at the sample, and probability that neutrons scattered at x will penetrate the rest of the sample. By integrating this expression from $x=0$ to $x=t$ and dividing by the counter area A, one obtains the flux at the detector due to all neutrons singly-scattered in the sample into the detector(I_1):

$$I_1=(\pi O/4)(D/L_1L_2)^2 nt\sigma_n(O^0)\exp(-nt\sigma_T). \quad (9)$$

Since the flux with sample out is simply $I_0=Q/L^2$, one obtains immediately in-scattering transmission

$$T_1=I_1/I_0=(\pi/4)(DL/L_1L_2)^2 nt\sigma_n(O^0) \times\exp(-nt\sigma_T). \quad (10)$$

In general, total cross section is given by

$$\sigma_T=(1/nt)ln(1/T)$$

$$\Delta\sigma_T=-(1/nt)(\Delta T/T). \quad (11)$$

For the present case, setting $\Delta T=T_1$ and true transmission $T=\exp(-nt\sigma_T)$

$$\Delta\sigma_T=(\pi/4)(DL/L_1L_2)^2\sigma_n(O^0). \quad (12)$$

Thus the apparent relative decrease in the total cross section from its true value σ_T due to the single in-scattered flux is

$$(\Delta\sigma_T/\sigma_T)=(\pi/4)(DL/L_1L_2)^2[\sigma_n(O^0)/\sigma_T]. \quad (13)$$

Using the above equation, one can obtain the true cross section σ_T from the apparent cross

section σ_T' from

$$\sigma_T=\sigma_T'/[1-(\Delta\sigma_T/\sigma_T)]. \quad (14)$$

If it is possible to keep the ratio D/L_1 constant by varying the sample diameter D, the minimum in-scattering correction is then easily found by making L_2 equal to L. These conditions can be easily realized by setting the sample position just in front of the Li neutron source[7].

4) B^{10} and NaI(Tl) Detector Assembly

Due to the low efficiency of scintillators for conversion of the energy of the interacting particle into light(=5%) and the unfavorable nonlinear response to low energy heavy charged particles in the organic phosphores, the use of a proton recoil scintillator system is restricted to energies above 80 keV. For lower energy neutrons it is necessary to provide energy for the detection device by means of nuclear reaction. Also another restriction to fast neutron measurement is that the neutron thermalization device before the detection event can not be used. Bollinger and Thomas[8] described a detector utilizing the B^{10} $(n, \alpha\gamma)$ Li^7 reaction with 0.4 μ sec resolving time. The long resolving time arises from the necessity for thermalization of the neutron to allow absorption by the rather small concentration of B^{10} allowable in the phosphore. This same nuclear reacton has been used by Newson and Gibbons[3] for fast detection of neutrons in the keV region but they kept the B^{10} slab separate from the γ-detecting scintillation counter. Utilizing of the γ-ray for the detection of these reactions permits the use of relatively thick sections of reaction originating material. For the efficient detection of the γ-ray, NaI (Tl)or some other dense high Z scintillator is required. The yield of 478-keV γ-rays representing the fraction of the particles from $B^{10}(n, \alpha\gamma)$ Li^7 which go to the excited state of L_i^7 is 95 percent for thermal energy neutrons and is not much different at energies in the keV region. By employing 95 percent enriched B^{10} compacted to 85 percent of the theoretical crystal density, about 100 percent efficiency for absorption of fast neutrons has been reported by Neiler and Good[9] at 5 keV with a 1 cm thick slab.

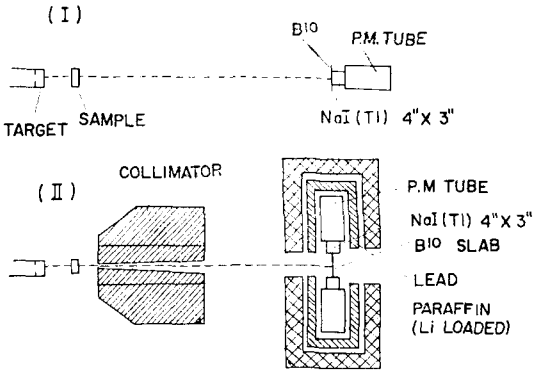

Fig. 4. Spectrometer with B^{10} slab detectors

The I^{127} in NaI (Tl) scintillator introduces the time-correlated background by prompt neutron capture γ-rays and radioactive iodine nuclei emitts β-rays with about 25 min. half-life; also these γ-rays fall into the 478 keV window in single channel analyzer. Hence, it is desirable not to face the NaI scintillation crystal at the incident neutron beam. In the present experiment the 92% enriched B^{10} slab of 12cm×12cm×0.5 cm is surrounded by four heavily shielded 4″×3″ NaI(Tl) scintillation crystal detectors connected in parallel, and mounted perpendicular to the neutron beam. Lithium-loaded-parraffin and lead bricks are used for detector shielding against incident and scattered neutrons from the environment.

Neutrons are detected by the B^{10}-four NaI assembly, where the 478-keV γ-rays from B^{10} $(n, \alpha\gamma)$ Li^7 are detected by these four NaI crystal of 4″ diameter, 3″ thickness which are coupled by XP 1040 photomultiplier tubes and with it 2π geometry is covered. Figure

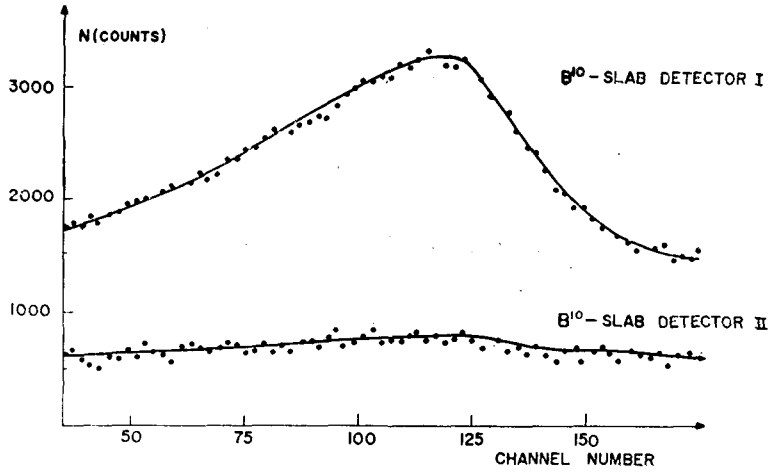

Fig. 5. Time corelated bacground for two time-of-flight spectrometers with B^{10}-slab detector

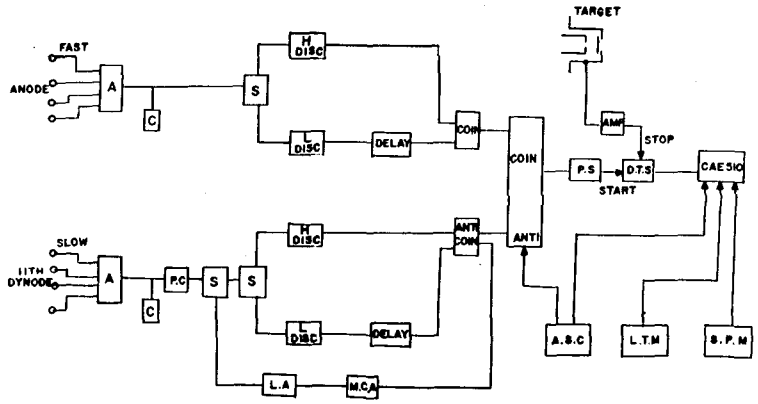

Fig. 6. Block diagram of electronics for B^{10}-slab time-of-flight spectrometer

4 shows a schematic section view of an arrangement using $B^{10}(n, \alpha\gamma)Li^7$+NaI which was used in the present experiment.

This results in a background which is vertually time-uncorrelated and furthermore much lower than in the conventional set up, where the scintillator is placed directly behind the B^{10}-slab[1].

Results of background measurement with these two kind of B^{10}-NaI arrangement are given in Figure 5, and Figure 6 illustrats the associated electronics. The over-all time-resolution of the system (excluding B^{10} slab thickness) is about 2.4 nsec for a 5m flight path measured by the time width of γ-rays from $Li^7(p, p'\gamma)$ originating in the target. It should be noted that this is the identical γ-ray to the one used in neutron detection B^{10} $(n, \alpha\gamma)$ Li^7. These same γ-rays serve to calibrate the time scale in that they cause the zero-time pulse.

3. The One-channel Multi-level Approximation

Some simple approximations in the theory of resolved and statistical resonance neutron nuclear reactions rely on the R-matrix theory as basic theoretical frame-work. The R-matrix theory has been developed by Wigner and Eisenbud[10] and exhaustively reviewed by Lane and Thomas[11]; a very useful more recent review elaborating in a simple manner particularly the physical content of the theory is

due to Vogt[12].

In neutron nuclear reactions the one-channel special case is most nearly realized for nuclei of medium weight isotopes like those of Na, Al, Ca, Ti, Cr, Fe, Ni *etc.* Almost all of these nuclei have the first inelastic scattering threshold only at energies above several hundreds keV. Below these thresholds many resonances are observed for which the only reaction remaining with elastic neutron reemission is neutron capture. The capture widths of these resonances, however, are generally so small compared to the neutron widths (except for some higher l-wave resonances). In the analysis of observed total neutron cross sections, they can safely be neglected and the elastic scattering cross section in very good approximation can be identified with the total cross section. The elastic scattering cross section is then given by

$$\sigma_n=\frac{2\pi}{k^2}\sum_{\ell J_j} g_J\{1-Re(U_{nj\ell,\,nj\ell}{}^{J})\} \tag{15}$$

where

k: wave number of the neutron,

g_J: spin statistical factor$=(2J+1)/2(I+1)$

J: total angular momentum

I: target spin

$U_{c,c'}$: Collision matrix

where the collision matrix has been simplified to the collision function

$$U_{nj\ell,Jn'j'\ell'}=e^{-2i\phi_\ell}\left\{1+2i\phi_{\ell'}\cdot\frac{R_{nj\ell,\,nj\ell}{}^{J}}{1-L_{\ell'}{}^{0}\cdot R_{nj\ell,\,nj\ell}{}^{J}}\right\} \tag{16}$$

where

ϕ_ℓ: hard sphere scattering phase shift

$R_{c,c'}$: R-matrix

L^0_ℓ: L_c-B_c

$L_c=S_c+iP_c$

S_c: shift factor

P_c: penetration factor

B_c: logarithmic derivative of the internal wave function at the channel surface, multiplied by the channel radius r_c.

γ^2_λ: reduced width

E_λ: λ-th resonance energy

Γ_λ: level width

and the R-matrix to the R-function

$$R_{nj\ell,\,nj\ell}{}^{J}=\sum_\lambda\frac{(\gamma_\lambda{}^{J}{}_{nj\ell})^2}{E_\lambda-E}\ . \tag{17}$$

As we are dealing only with neutron reactions, we omit the lower index n in k_n.

With the abbreviation

$$X^J{}_{nj\ell}=\frac{1-(S_\ell-B_\ell)R_{nj\ell,\,nj\ell}{}^{J}}{P_\ell\cdot R_{nj\ell,\,nj\ell}{}^{J}} \tag{18}$$

evaluation of the real part of U from the Equation 16 and its insertion into the Equation 15, one gets for elastic scattering cross section

$$\sigma_n=\frac{4\pi}{k^2}\sum_{\ell J i}g^J\ \sin^2\phi_\ell + \frac{4\pi}{k^2}\sum_{\ell i}g_J\left\{\frac{\cos 2\phi-X^J{}_{nj\ell}\sin 2\phi_\ell}{1+(X^J{}_{nj\ell})^2}\right\} \tag{19}$$

Equation 19 is exact as long as all other channels except the elastic scattering channel can be neglected. For the application of this equation to the interpretation of observed pure scattering resonances the boundary condition parameters. B_ℓ have to be specified. It is shown that, as long as $x=KR\ll 1$, the level shifts

$$\Delta^J{}_{\lambda nj\ell}=-(S_\ell-B_\ell)\gamma^2{}_{\lambda nj\ell}{}^{J} \tag{20}$$

can be made very nearly to vanish for all resonces in a certain restricted energy range for the special choice

$$B_\ell=S_\ell(E_r). \tag{21}$$

Here E_r is one of the resonances observed in this range corresponding to the internal eigen values E. This choice of B_ℓ causes E to coincide with E_r and the other eigenvalue $E_\lambda \neq E_\lambda$ to become very nearly equal to the observed resonances $E_s \neq E_r$. For s-wave resonances

$$\Delta^J{}_{\lambda nj_0}\equiv 0\ . \tag{22}$$

For the resonances in medium weight nuclei considered, the condition $kR\ll 1$ is usually fulfilled. Thus we have

$$X^J{}_{njl} \cong \frac{1}{P_l \cdot R_{njl^J,njl}} = \frac{2}{\sum_r \frac{\Gamma_{rnjl^J}}{E_r - E}} \quad (23)$$

exactly valid for $l=0$ and in very good approximantion valid for $l>0$ resonances. With Equation 23
and

$$\sum_{Jj} g_J = \sum_{J=|l-j|}^{l+j} \sum_{j=|J-\frac{1}{2}|}^{J+\frac{1}{2}} g_J = 2l+1 \quad (24)$$

we get for σ_n in detailed notation

$$\sigma_n = \frac{4\pi}{k^2} \sum_{l=0}^{\infty} (2l+1)\sin^2\phi_l + \frac{4\pi}{k^2} \sum_{l=0}^{\infty} \sum_{J=|l-j|}^{l+j} \sum_{j=|J-\frac{1}{2}|}^{I+\frac{1}{2}} g_J \times \left\{ \frac{\left(\sum_r \frac{\Gamma_{rnjl^J}}{2(E_r-E)}\right)^2 \cos 2\phi_l - \sum_r \frac{\Gamma_{njrl^J}}{2(E_r-E)} \sin 2\phi_l}{1+\left(\sum_r \frac{\Gamma_{nrjl^J}}{2(E_r-E)}\right)^2} \right\}. \quad (25)$$

The first term is the potential scattering cross section, the second term is composed of resonance scattering and interference cross sections. In practical applications the R-function, Equation 17, is split into contributions from the resonances investigated in a restrcited energy range and those not explicitely considered from levels outside this range (R^{∞})

$$R = R_{\infty} + \sum_{\lambda}^{\infty} \frac{\gamma_\lambda^2}{E_\lambda - E} \cong R_{\infty} + \sum_r \frac{\gamma^2{}_r}{E_r - E} \quad (26)$$

According to Lane and Thomas[11] this does not change the form of the cross section expression, but only the ϕ_l, P_l and S_l:

$$\phi_l \to \phi_l = \text{arctg}\left(\frac{F_l}{G_l}\right) - \text{arctg}\left(\frac{R_{\infty} P}{1 - R^{\infty} S_l}\right) \quad (27a)$$

$$S_l \to S_l = \frac{S_l(1-R^{\infty}S_l) - R^{\infty}P_l^2}{(1-R^{\infty}S_l)^2 + (R^{\infty}P_l)^2} \quad (27b)$$

$$P_l \to P_l = \frac{P_l}{(1-R^{\infty}S_l)^2 + (R^{\infty}P_l)^2} \quad (27c)$$

The function F_l and G_l are special functions defined elsewhere.[14]

The one-channel multi-level formula(Equation 19) particularly in the Duke work[14], has proven to be capable of a correct description

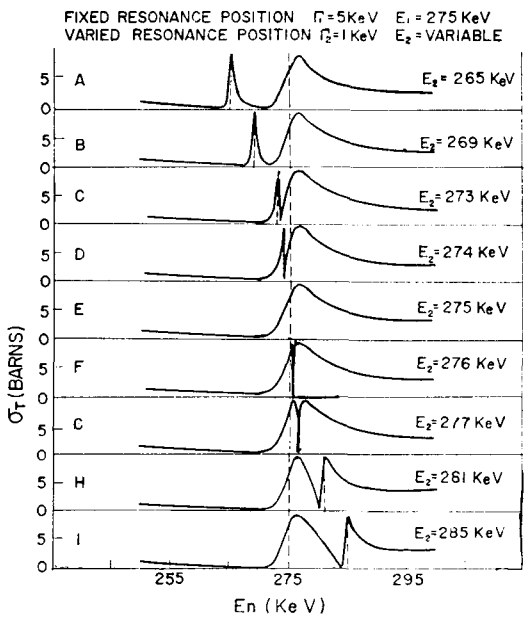

Fig. 7. Two level interference. The multilevel formula described in the text has been used to illustrate the coherent interference effects of two resonances in the same channel. A resonance 1keV wide is shown at varios positions relative to a wider resonance fixed at 275KeV. The parameter R^{∞} and the nuclear radius, A, used in the multilevel calculation are typical of the Nuclei near A=50

of the very complicated scattering resonance structure of medium weight nuclei. In particular it describes correctly the interference between two closely spaced resonances with the same quantum numbers which destroys the single level shape of both resonances in an often observed characteristic way. This is illustrated by Figure 7 calculated by the so-called FANAL-IR computer code with Bowman's resonance parameters. One of the two resonances shown has a fixed position at E_1= 275 keV and a width Γ_1=5 keV. The position E_2 of the other smaller resonance(Γ_2=1 keV) is varied through E_1 from 265 to 285 keV and the resulting cross section shape is shown for several relative positions of both resonances. Note particularly the drastic change in the shape of the smaller resonance when crossing

the large one. We note only one further important property of this equation. For $E=E_r$, σ_n becomes simply

$$\sigma_n = \sigma_p + \frac{4\pi}{k^2} g_J \cos 2\phi_\ell \tag{28}$$

with

$$\sigma_p = \frac{4\pi}{k^2} \sum_{\ell=0}^{\infty} (2l+1)\sin^2\phi_\ell. \tag{28a}$$

Equation 28 can be used, after subtraction of the potential scattering to determine, through g_j, the total angular momentum J of the r-th resonance. In the practical application of Equation 25 to the interpretation of an observed resonance structure, the E_r and Γ_{rn} are thus free parameters which have to be chosen and varied so as to describe best the observed cross section. The interpretation is rendered difficult by the fact that the neutrons used in the cross section measurements are not monoenergetic, but distributed more or less in energy. For the observed resonance structure, one has therefore to take into account the cross section expression Equation 25 including the neutron energy resolution function in the calculations. Contray to this, the Doppler broadening particularly of the large s-wave resonances of medium weigh tnuclei can be neglected, as the Doppler width Δ is very small compared to Γ.[15]

4. Analysis of Experimental Data (FANAL-IR code)

For reliable resonance parameters, the multi-level formula which result from the R-matrix formalism[14] is programmed for the IBM 360/65 computer, a so called FANAL-IR code. The programme is able to accomodate a maximum of 50 resonances for each spin system for a mixture of three different isotopes, considering s-and p-waves only. The computing time is about 10 min. for 1000 data points of the transmission curve. An energy-dependent correction term for the phase shift is assumed in order to approximate the influence of the unkown resonances outside the measured range[15]. This term is found to change only slowly over the greatest part of the range, but is strongly energy dependent near the energy limits of the measured spectrum showing the importance of outside resonances. The influence of the resonances outside the analysed region is taken into account using a scattering phase of the form

$$\varphi_{o\ell} = ka(1-R^{\infty}_{oJ}) \tag{29}$$

where

$$R^{\infty}_{oJ} = A_J + B_J(E-E_m) + C_J(E-E_m)^2. \tag{30}$$

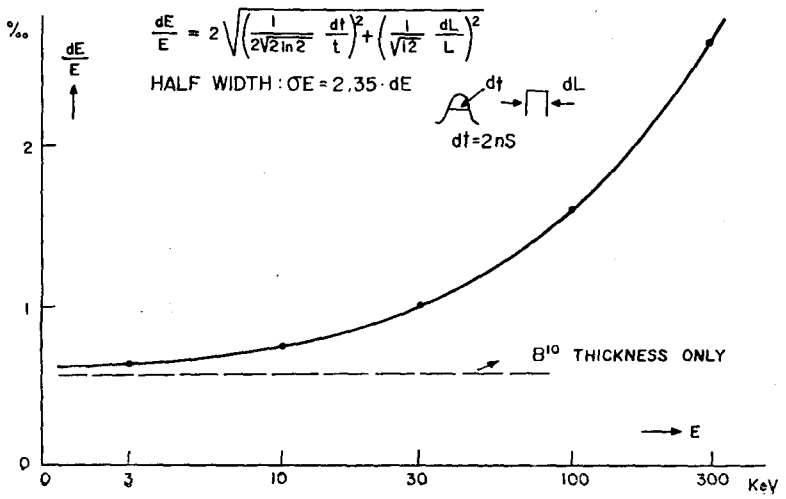

Fig. 8. Energy resolution of the spectrometer

Here k is the wave number, a the nuclear radius and E_m the middle of the energy interval analysed. The coefficients A_j, B_j, and C_j are chosen to give the best fit in valleys between resonance peaks.

The finite resolution of the spectrometer is accounted for by modulating the multi-level formula with the experimental resolution function. This resolution function could be very well approximated by assuming a Gaussian form. This type of resolution function fits well with the experimental cross section curve.

To extract the resonance parameters from the experimental cross section, tentative parameters are assigned for each peak for the first iteration. The calculated cross section are then compared with the experimental data by means of the least square analysis and then parameters are automatically adjusted until a satisfactory agreement is obtained.

5. Experimental Results and Discussion

The over-all Energy resolution is given in Figure 8

Total cross sections of the following isotopes were measured in the energy range of 8 to 80 keV, as previously reported[16],

Fe^{54}: Fe_2O_3 powder enriched 97.69% Fe^{56} Natural Iron.

Ti^{47}: TiO_2 powder enriched 79.5%(16.5% Ti^{48}).

Ni^{47}: Metal powder enriched 91.78%(5.25 Ni^{60}).

All sample material was provided by the EANDC-pool. The materal is filled into thin-walled Al containers. In the measurements without sample, equivalent empty containers were used. Different sample thickness, depending on the energy range and the cross section structure, were chosen in order to get optimal statistical error and in-scattering conditions. As the cross section of oxygen, 3.5 barns, is constant up to 300 keV, the correction for the oxygen content of the sample is easily carried out.

Figure 9 shows the total cross sections of Ti^{47} with the ORNL recent measurement[1] for comparison. Figure 10 shows the total cross section of Ni^{61} also with the reference. It is also possible to assign a spin state for each resonance by means of peak and inter ference dip. Figures 11, 12, 13 show the distribution of neutron width of Ni^{61} for each

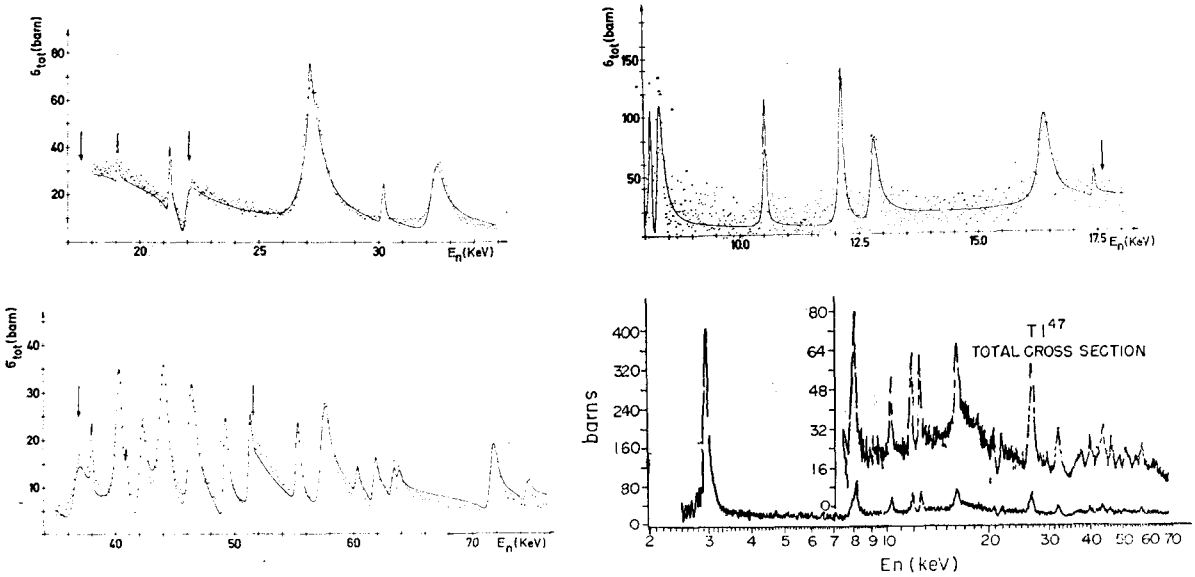

Fig. 9. Comparison of cross section curve for Ti^{47}

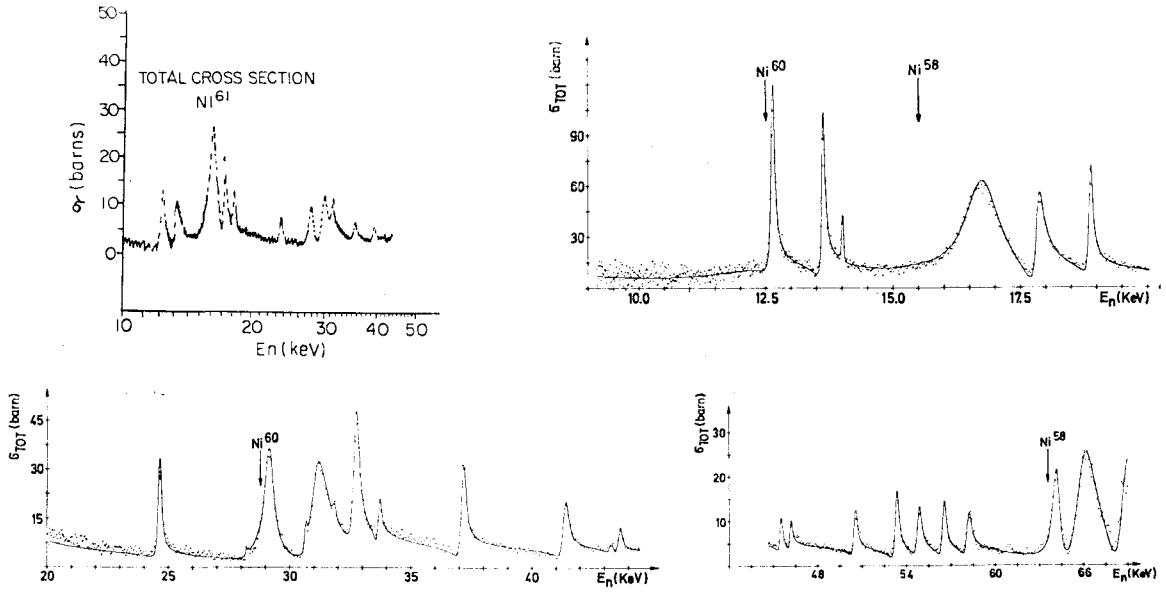

Fig. 10. Comparison of cross section curve for Ni^{61}

Table 1. Resonance parameters of Ti^{47}

E_λ*		J	$2g\Gamma_\lambda$ *)		$2g\Gamma^\circ_\lambda$ (eV)		E_λ *		J	$2g\Gamma_\lambda$ *		$2g\Gamma^\circ_\lambda$ (eV)	
Present	BNL		Present	BNL	Present	BNL	Present	BNL		Present	BNL	Present	BNL
8.14		2	0.055		0.610		40.37		3	0.807		4.017	
8.32	8.32	2	0.122	0.100	1.338	1.1	41.03		2	0.048		0.237	
10.54	10.51	3	0.068	0.06	0.663	0.6	42.08	42.1	3	1.027	0.270	5.007	1.3
12.13	12.12	3	0.140	0.08	1.272	0.72	42.23	43.8	2	0.484	0.560	2.356	2.7
12.16		2	0.018		0.164		44.40	46.1	3	0.823	0.480	3.822	2.3
12.81	12.82	2	0.146	0.08	1.290	0.74	49.27	49.2	3	0.367	0.370	1.654	1.7
16.36	16.40	3	0.462	0.185	3.613	1.45	51.34	52.1	3	0.210	0.085	0.927	0.4
17.39		2	0.042		0.319		55.37	54.0	3	0.322	0.223	1.369	0.96
19.08		3	0.023		0.167		57.56	56.2	3	1.002	0.530	4.178	2.2
21.26		2	0.052		0.357		60.29		2	0.074		0.302	
27.12	27.0	2	0.092	0.700	0.559	4.4	61.78		2	0.177		0.713	
27.17		3	0.116		0.704		63.37		3	0.113		0.449	
30.18		2	0.062		0.357		63.80		3	0.062		0.246	
32.33	32.3	2	0.498	0.500	2.770	2.8	71.68		3	0.571		2.134	
38.11	39.1	3	0.093	0.370	0.477	1.9	74.55		2	0.107		0.392	

* keV Uncertainty in Γ from the various sources of error: 4.78%

spin state and the agreement with the Porter-Thomas disiribution. Resonance parameters of Ti^{47} and Ni^{61} are given in Table 1 and 2 with BNL value[17] for comparison, and Table 3 shows the various statistical parameters. The resonances are sufficiently broad to be unaffected by Doppler broadening and resolution. Also they are almost purely elastic scattering resonances, so that their total angular momentum values can be ascertained immediately from the peak cross sections. using the g-factor in Equation 15. The grouping of spins is confirmed by the apparent resonance-resonance interference, and the absence of a

Table 2. Resonance parameters of ^{61}Ni

E_λ *		J	$2g\Gamma_\lambda$ *		$2g\Gamma^\circ_\lambda$ (eV)		E_λ *		J	$2g\Gamma_\lambda$ *		$2g\Gamma_\lambda^\circ$ (eV)	
Present	BNL		Persent	BNL	Present	BNL	Present	BNL		Present	BNL	Present	BNL
7.15	6.97	1	0.056	0.023	0.663	0.28	33.68	33.8	1	0.044	0.123	0.240	0.67
7.55	7.37	2	0.221	0.238	2.544	2.79	37.13	36.0	2	0.166	0.294	0.602	1.55
8.74		2	0.008		0.086		41.34	40.0	1	0.132	0.243	0.650	1.21
12.64	12.4	2	0.094	0.068	0.837	0.61	43.25	42.2	2	0.013	0.133	0.063	0.65
13.63	13.3	2	0.076	0.076	0.651	0.66	43.61	44.0	2	0.038	0.169	0.182	0.80
14.02	13.7	1	0.013	0.013	0.110	0.11	45.49		1	0.050		0.235	
16.70	16.3	1	0.613	0.411	4.744	3.21	46.16	48.4	1	0.041	0.083	0.191	0.38
17.86	17.5	1	0.133	0.174	0.996	1.32	50.51		1	0.100		0.445	
18.87	18.3	2	0.086	0.181	0.626	1.34	53.30		2	0.176		0.763	
24.62	23.8	1	0.097	0.100	0.619	0.64	54.81		1	0.142		0.607	
28.21	28.2	2	0.004	0.236	0.024	1.40	56.49		2	0.149		0.627	
29.11		1	0.307		1.800		58.16		1	0.134		0.556	
30.64	30.2	2	0.016	0.423	0.092	2.43	64.07		2	0.669		2.644	
31.13	31.6	1	0.591	0.392	3.350	2.20	65.87		2	1.788		6.968	
31.83		2	0.010		0.056		68 77		2	1.375		5.245	
32.70	32.7	2	0.275	0.120	1.521	0.66							

* keV

Uncertainty in Γ from the various sources of error: 4.78%

Table 3. Averaged values

Target nucleus	Spin state	Enery range (keV)	D(keV) a	D(keV) b	Γn°(eV) a	Γn°(eV) b	$S\times10^4$ a	$S\times10^4$ b	Number of -levels a	Number of -levels b
Ti^{47}	J=2	8—76	5.11	3.04	1.0	0.6	2.0	2.1	14	24
	J=3		4 08	2.95	2.0	1.4	4.8	4.9	16	22
	Independent		2.29	1.59	1.6	1.1	3.5	3.6	30	43
Ni^{61}	J=1	7—69	3.92	2.79	1.4	1.0	3.7	3.7	14	20
	J=2		3.83	2.44	1.1	0.7	2.9	3.0	17	27
	Independent		2.05	1.36	1.3	0.9	3.1	3.2	31	47

a. Only Number of Analyzed levels used

b. "Missed levels" included

strong dip immediately before resonance signifies that the resonance has a different spin from the pre-placed resonance. These spin values are also given Table 1 and Table 2.

The weak spin dependency of strength function are shown in Table 3 but they have an opposite tendency on the spin value.

Also the transmission curves of Fe^{54} and natural iron are given in Figures 14, 15 and 16 which show rather well the fine structure of resonance of Fe^{54} around 54 keV. From these experiments, resonance energies are assigned to Fe^{54} at 7.93, 53.3 and 71.9 keV, and Fe^{56} at 27.9, 52.1, 74.0 and 83.8 keV. Several weak resonances are observed in these trans mission curves. There is a discrepancy between the present results and BNL value[17] for 54 keV resonance of Fe^{54}. This arises from the high resolution of the present experiment and the high purity sample material.

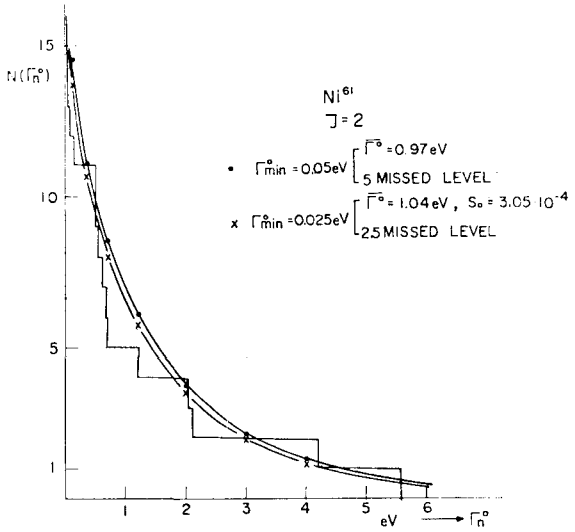

Fig. 11. Distribution of the reduced neutron width for Ni^{61} (J=2)

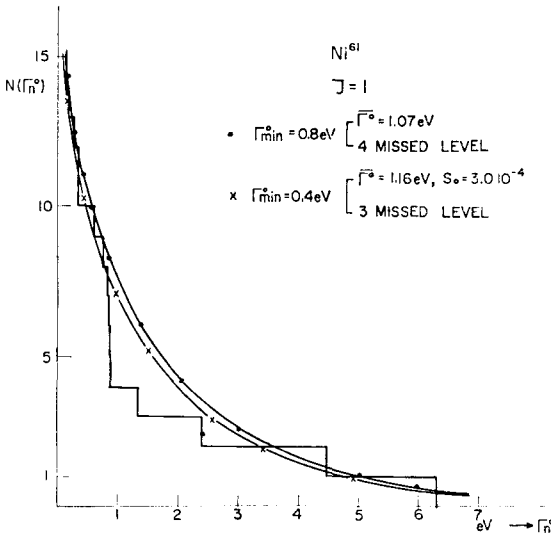

Fig. 12. Distribution of the reduced neutron width for Ni^{61} (J=1)

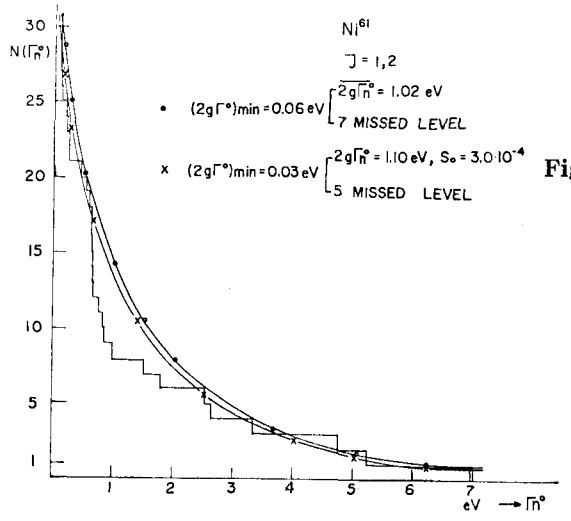

Fig. 13. Distribution of reduced neutron width for Ni^{61} (Spin-independent)

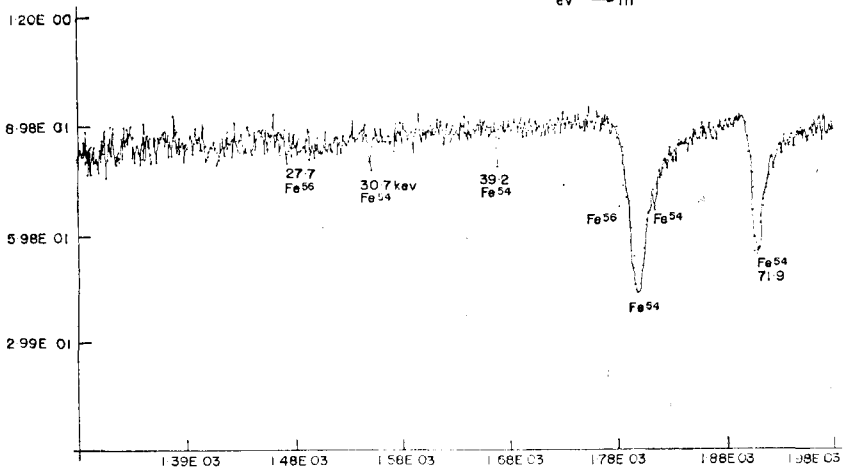

Fig. 14. Trnmission of Fe^{54}-thin

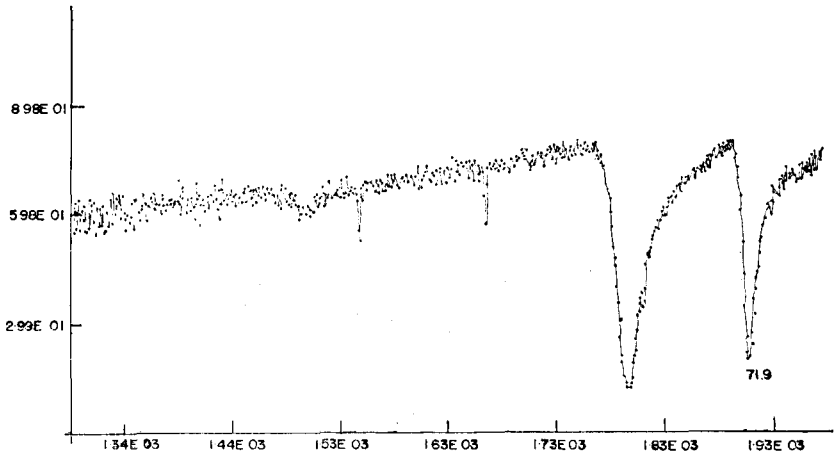

Fig. 15. Transmission of Fe^{54}-thick

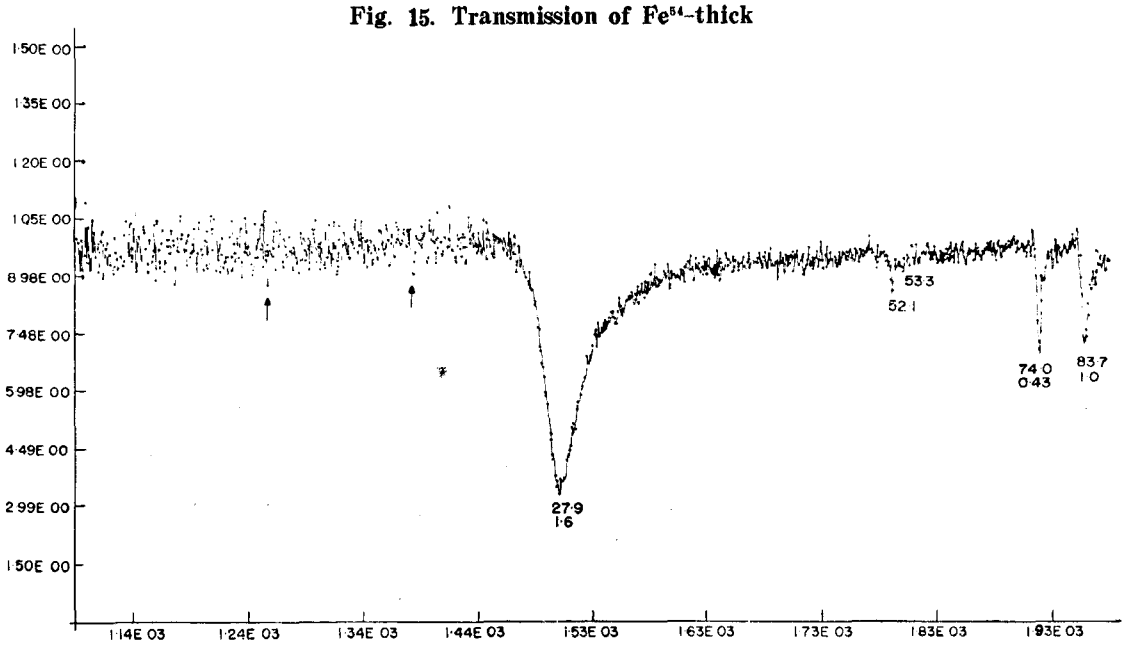

Fig. 16. Transmission of natural iron

Energy resolution, better than 0.3% at 50 keV, is obtained from the best fit of the observed cross sections using the resolution broadening effects around the cross section peaks.

Using the Equation 19 and resolution broadening, this high resolution reproduces the good fits of the observed cross sections for the determination of reliable resonance parameters and spin values of 30 resonances of Ti^{47} and 31 resonances of Ni^{61} up to 80keV.

Acknowledgment

The auther wishes to thank Professors P. Y. Pac and H. I. Bak for their interest in this work and for helpful discussion, and also to acknowledge the generous help of the entire Van de Graff group at Karlsruhe, and especially the cooperation and help of Doctors F. Froehner and K-N. Mueller in the excution

and analysis of this experiment. The auther is also indebted to Professor R. G. Sauer for the preparation of the manuscript.

References

1) W. M. Good, *et al.*, Phys. ReV. **151**, 912(1966)
2) J. B. Garg, *et al.*, CR-1860 (1964)
3) H. W. Newson and J. H. Gibbons, Fast neutron Physics, 11. Chap. V. L. (1963)
4) R. L. Macklin and J. H. Gibbons, Phys. Rev. **109**, 105 (1958)
5) G. Bruedermuller and P. Wahl, KFK-IAK Bericht, No. 40 (1962)
6) J. P. Cooner, Phys. Rev. **109**, 1268 (1958)
7) C. Cierjack Proc. 2nd Intern. Conf. on Nuclear Data for Reactor at Helsinki **2** 219(1970)
8) L. Bollinger, Proc. Inern. Conf. Peaseful Uses of Atomic Energy. Geneva, **4**, 47 (1956)
9) J. H. Neiler and W. M. Good, Fast neutron Physics I. IV. A. (1960)
10) E. P. Wigner and L. Eisenbud, Phys. Rev. **72**, 29 (1947)
11) A. M. Lane and R. G. Thomas, Rev. Modern Phys. **30**. 257 (1958)
12) E. Vogt, Revs. Modern Phys. **34**, 723 (1962)
13) F. W. K. Firk, *et al.*, Proc. Phys. Soc. **82**, 477 (1963)
14) C. D. Bowman, *et al.*, Ann. of Phys. **13**. 319 (1962)
15) J. E. Lynn and E. R. Rae, J. Nuclear Energy 1, **4**, 418 (1957)
16) M. Cho, *et al.*, J. of Korean Nuclear Society, **2**, 241 (1970)
17) M. D. Goldberg *et al.*, BNL 325 Supplement No. 2, Neutron cross section, **IIA** (1966)